Solid State Sciences 11 (2009) 1137–1143

Contents lists available at ScienceDirect

Solid State Sciences

journal homepage: www.elsevier.com/locate/ssscie

Structure and properties of α-$AgFe_2(MoO_4)_3$

L. Balsanova [a,b], D. Mikhailova [a], A. Senyshyn [a], D. Trots [a,1], H. Fuess [a], W. Lottermoser [c], H. Ehrenberg [a,d,*]

[a] Institute for Materials Science, Darmstadt University of Technology, Petersenstr. 23, D-64287 Darmstadt, Germany
[b] Buryat State University, Ul. Smolina 24, 670000 Ulan-Ude, Russia
[c] University of Salzburg, Department of Materials Engineering & Physics, Hellbrunnerstr. 34, A5020 Salzburg, Austria
[d] Institute for Complex Materials, IFW Dresden, Helmholtzstr. 20, D-01069 Dresden, Germany

ARTICLE INFO

Article history:
Received 17 August 2008
Received in revised form
17 February 2009
Accepted 3 March 2009
Available online 14 March 2009

PACS:
61.66.Fn
75.50.Ee
91.60.Ed
61.10.Nz
61.12.-q

Keywords:
$AgFe_2(MoO_4)_3$
Antiferromagnetic structure
Anisotropic thermal expansion
Superexchange couplings
Mössbauer spectroscopy

ABSTRACT

Silver diiron tris(oxomolybdate), α-$AgFe_2(MoO_4)_3$, was synthesized in sealed silica tubes at 1050 K and is isostructural to α-$NaFe_2(MoO_4)_3$, determined by single-crystal X-ray diffraction (space group P−1, $a = 6.9320(7)$ Å, $b = 6.9266(6)$ Å, $c = 10.9732(13)$ Å, $\alpha = 81.197(8)^\circ$, $\beta = 83.456(9)^\circ$, $\gamma = 81.352(8)^\circ$ at 300 K, $Z = 2$). The crystal structure is built up from both monomers and edge-sharing dimers of $[FeO_6]$-octahedra, which are linked with each other by isolated $[MoO_4]$-tetrahedra to a three-dimensional network. Ag ions are situated on a site with four near oxygen neighbours. Thermal expansion is most pronounced along the *c*-axis, while the angle α decreases with increasing temperature. Antiferromagnetic ordering is indicated by a sharp maximum in the temperature dependence of magnetization at 21.5(5) K, and a magnetic moment of 5.36(1) μ_B per Fe-ion was derived from the Curie constant in the paramagnetic region. The collinear antiferromagnetic structure with propagation vector $\mathbf{k} = (0,½,½)$ and an ordered magnetic moment of 4.62(9) μ_B per Fe-ion were deduced from neutron powder diffraction data and give evidence for an underlying magnetic interaction mechanism, resulting in rather strong and long-ranged couplings. Mössbauer spectroscopy shows a change in the electronic configuration on the two distinct Fe sites between room temperature and 150 K, accompanied by an increase of the average Fe–O distance for one site and a shrinking one for the other as expected for charge ordering in a mixed valence compound with Fe(II) and Fe(III).

1. Introduction

Crystal structures and properties of quaternary phases in the system Na–Fe–Mo–O have been studied in detail [1–4]. Five different phases with three-dimensional networks of isolated $[MoO_4]$-tetrahedra and $[FeO_6]$-octahedra could be established: $NaFe(MoO_4)_2$, α-$NaFe_2(MoO_4)_3$, β-$NaFe_2(MoO_4)_3$, $Na_3Fe_2(MoO_4)_3$, $NaFe_4(MoO_4)_5$. In addition to these ortho-oxomolybdate phases, a new phase with the formula $Na_3Fe_2Mo_5O_{16}$ and with layers of Mo_3O_{13} clusters consisting of $[MoO_6]$-octahedra was synthesized and characterized [4]. The systematic investigation of structures and properties of such quaternary phases of an alkaline metal, a 3d-transitional metal, molybdenum and oxygen was now extended to compounds with Ag instead of an alkaline metal. Several analogues are expected in the light of similar ionic radii and coordinations of Ag and Na. However, only $AgFe(MoO_4)_2$ is reported in literature [5]. The preparation, structure and properties of a new quaternary Ag–Fe–Mo–O phase, namely α-$AgFe_2(MoO_4)_3$, are described.

2. Experimental

2.1. Synthesis

α-$AgFe_2(MoO_4)_3$ was synthesized in a sealed silica tube from the educts Ag_2MoO_4, Fe_2O_3 (Aldrich, 99.98%), FeO (Aldrich, 99.9%) and MoO_3 (Johnson Mattey, Grade A1) in molar ratios 1:1:2:5. The reactants were mixed in an agate mortar under acetone, and a pressed pellet was sealed in an evacuated quartz tube and heated at 973 K for 2 days.

2.2. Single-crystal X-ray diffraction

The crystal structure of α-$AgFe_2(MoO_4)_3$ was solved from single-crystal X-ray diffraction data using the Xcalibur system from Oxford

* Corresponding author. Institute for Complex Materials, IFW Dresden, Helmholtzstr. 20, D-01069 Dresden, Germany. Tel.: +49 351 4659 246; fax: +49 351 4659 9 246.
E-mail address: h.ehrenberg@ifw-dresden.de (H. Ehrenberg).
[1] Current address: Hamburger Synchrotronstrahlungslabor, Notkestr. 85, D-22607 Hamburg, Germany.

1293-2558/$ – see front matter © 2009 Elsevier Masson SAS. All rights reserved.
doi:10.1016/j.solidstatesciences.2009.03.006

Table 1
Details of X-ray single-crystal data collection and structure refinement for α-$AgFe_2(MoO_4)_3$.

Crystal data		
Chemical formula	$AgFe_2Mo_3O_{12}$	
Formula weight (g/mol)	699.39	
Crystal system	Triclinic	
Space group	$P\bar{1}$	
Unit cell dimensions	$a = 6.9320(7)$ Å,	$a = 6.9222(6)$ Å,
	$\alpha = 81.197(8)^\circ$,	$\alpha = 81.573(7)^\circ$
	$b = 6.9266(6)$ Å,	$b = 6.9168(5)$ Å,
	$\beta = 83.456(9)^\circ$	$\beta = 83.562(8)^\circ$
	$c = 10.9732(13)$ Å,	$c = 10.9001(11)$ Å,
	$\gamma = 81.352(8)^\circ$	$\gamma = 81.448(7)^\circ$
Cell volume (Å^3)	512.52(9)	508.33(8)
Z	2	
Calculated density (g/cm^3)	4.532	4.569
Temperature (K)	300(2)	104(2)
Crystal form, colour	Prism, black	
Crystal size (mm^3)	$0.100 \times 0.085 \times 0.055$	
Data collection		
Diffractometer	Oxford Diffraction Xcalibur (TM); single-crystal X-ray diffractometer with sapphire CCD detector	
Data collection method	Rotation method data acquisition using ω and φ scans(s)	
Radiation type	Mo-Kα ($\lambda = 0.71073$ Å)	
Absorption coefficient (mm^{-1})	8.246	8.313
$F(000)$	642	
θ range for data collection	2.99–27.67°	2.99–27.66°
Range of h, k, l	$-8 \le h \le 9$, $-8 \le k \le 8$, $-14 \le l \le 13$	$-8 \le h \le 8$, $-8 \le k \le 8$, $-13 \le l \le 13$
Reflections collected/ unique	6428/2202	6352/2182
Completeness to $\theta = 26.37^\circ$	99.6%	99.5%
Refinement method	Full-matrix least-squares on F^2	
Data/restraints/ parameters	2202/0/164	2182/0/164
Goodness-of-fit on F^2	1.086	1.054
Final R indices [$I > 2\text{sigma}(I)$]	$R1 = 0.0369$, $wR2 = 0.0793$	$R1 = 0.0215$, $wR2 = 0.0491$
R indices (all data)	$R1 = 0.0434$, $wR2 = 0.0821$	$R1 = 0.0257$, $wR2 = 0.0501$
Extinction coefficient	0.0031(3)	0.0029(2)
Largest diff. peak and hole	5.827 and −5.798 e/Å^3	2.879 and −2.670 e/Å^3

Diffraction. The software packages SHELXS [6] and SHELXL [7] were used for structure solution and refinement as included in X-STEP32 [8]. Details of the experimental conditions and the refinement process are summarized in Table 1 for the experiments at 300(2) and 104(2) K.

2.3. X-ray powder diffraction

Phase purity was checked by X-ray powder diffraction in flat-sample transmission geometry on a STOE STADI P diffractometer, equipped with a linear position-sensitive detector with 6° aperture. Mo-$K\alpha_1$ radiation was selected by a curved Ge(111) monochromator.

2.4. Synchrotron powder diffraction

The sample was sealed in a 0.3 mm quartz capillary and heated by a graphite rod in a STOE furnace. Temperature induced structural changes were followed by powder diffraction using the beamline B2 [9] at HASYLAB with the on-site readable one-dimensional position-sensitive detector OBI [10].

Table 2
Atomic coordinates ($\times 10^4$) and thermal displacement parameters (Å$^2 \times 10^3$) for α-$AgFe_2(MoO_4)_3$ at 104 K. U_{eq} is defined as one third of the trace of the orthogonalized U_{ij} tensor, and the anisotropic displacement parameters for α-$AgFe_2(MoO_4)_3$. The anisotropic displacement factor exponent takes the form: $-2\pi^2[h^2a^{*2}U_{11} + \cdots + 2hka^*b^*U_{12}]$.

Atom label	Fractional coordinates			U_{eq}
	x/a	y/b	z/c	
Mo(1)	−2397(1)	1006(1)	−1453(1)	3.38(10)
Mo(2)	−2838(1)	2808(1)	1835(1)	4.23(10)
Mo(3)	2804(1)	2950(1)	−4531(1)	3.46(10)
Fe(1)	−1819(1)	1752(1)	−4940(1)	3.79(13)
Fe(2)	−2278(1)	−2303(1)	1052(1)	3.76(13)
Ag(1)	−1456(1)	−4129(1)	−2217(1)	20.41(11)
O(1)	−1807(4)	−1532(4)	−795(3)	6.2(6)
O(2)	−2126(5)	4899(4)	813(3)	7.8(6)
O(3)	−630(4)	2573(4)	−1254(3)	7.4(6)
O(4)	−4806(4)	2022(4)	−978(3)	7.5(6)
O(5)	−1430(5)	2434(5)	3133(3)	8.4(6)
O(6)	−2284(5)	954(5)	−3039(3)	9.4(6)
O(7)	5210(4)	2105(5)	−5011(3)	8.7(6)
O(8)	1252(4)	1279(4)	−4883(3)	7.6(6)
O(9)	2611(5)	3018(5)	−2900(3)	9.6(6)
O(10)	2094(5)	5300(5)	−5325(3)	8.6(6)
O(11)	−5281(5)	3274(5)	2350(3)	11.3(7)
O(12)	−2463(5)	622(4)	1085(3)	9.0(6)

Table 3
Selected bond lengths [Å] for α-$AgFe_2(MoO_4)_3$ at 104 K.

Mo(1)	O(6)	1.727(3)	Mo(2)	O(11)	1.720(3)	Mo(3)	O(7)	1.730(3)
	O(4)	1.763(3)		O(5)	1.774(3)		O(10)	1.755(3)
	O(3)	1.800(3)		O(2)	1.787(3)		O(9)	1.774(3)
	O(1)	1.802(3)		O(12)	1.794(3)		O(8)	1.797(3)
Fe(1)	O(7)	2.043(3)	Fe(2)	O(2)	1.976(3)	Ag(1)	O(11)	2.263(3)
	O(6)	2.065(3)		O(9)	1.999(3)		O(3)	2.383(3)
	O(10)	2.079(3)		O(1)	2.008(3)		O(5)	2.504(3)
	O(5)	2.081(3)		O(4)	2.009(3)		O(1)	2.508(3)
	O(8)	2.108(3)		O(12)	2.013(3)			
	O(8)	2.109(3)		O(3)	2.027(3)			

Diffraction patterns have been collected in 20 K temperature steps with radiation of 0.75026(1) Å wavelength up to 800 K. One additional pattern was taken at room temperature after the heat treatment.

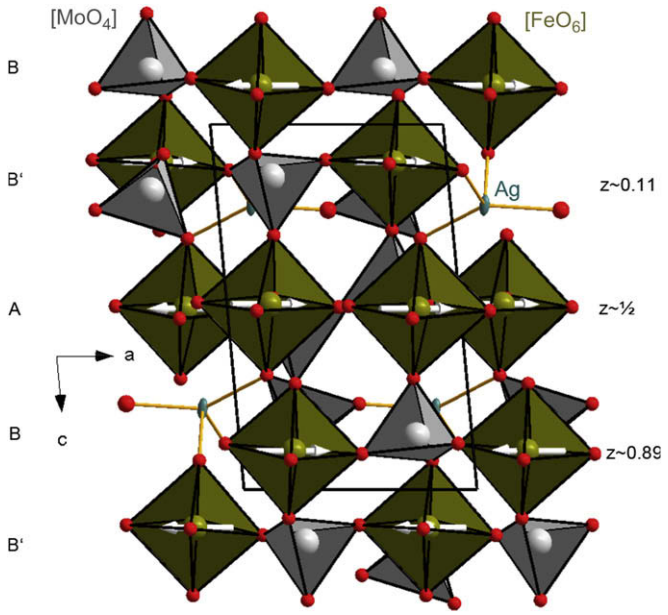

Fig. 1. Crystal and magnetic structure of α-$AgFe_2(MoO_4)_3$.

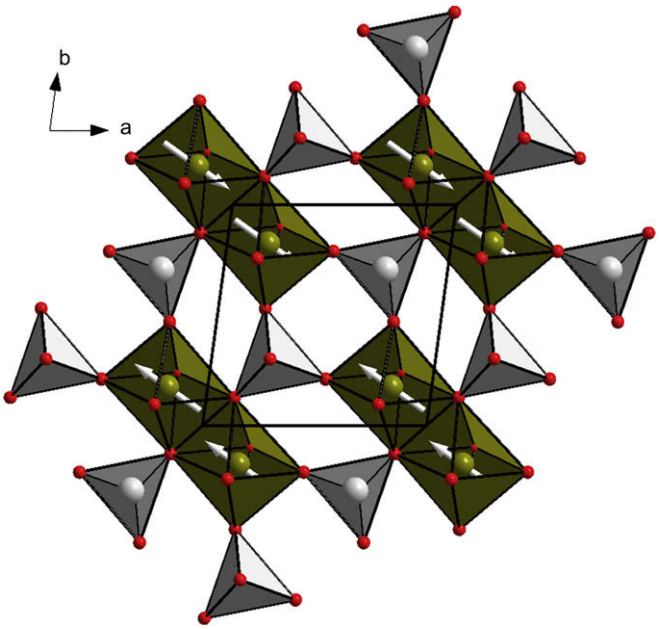

Fig. 2. Layer type A, $z \sim ½$.

2.5. Magnetization study

The magnetic properties of α-$AgFe_2(MoO_4)_3$ have been studied with a superconducting quantum interference device (SQUID) from Quantum Design. Measurements were performed in the temperature range from 1.8 to 350 K at a field strength of 50 Oe.

2.6. Neutron powder diffraction

Magnetic structure determination was based on neutron powder diffraction data obtained using SPODI [11] at the research reactor FRM II in Garching near Munich. The sample containing vanadium can was mounted in a cold-head cryostat, and two data sets at 50 K and 5 K, above and below the magnetic ordering temperature, respectively, were collected with monochromatic neutrons of 1.5481(1) Å wavelength.

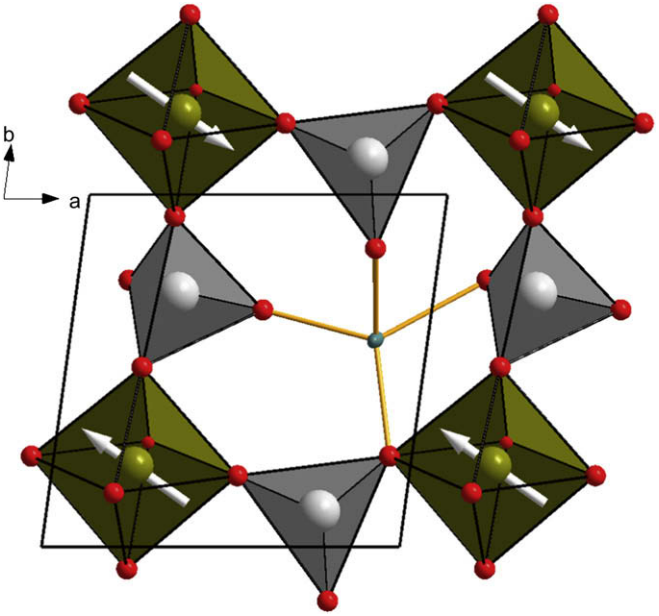

Fig. 3. Layer type B, $z \sim 0.89$.

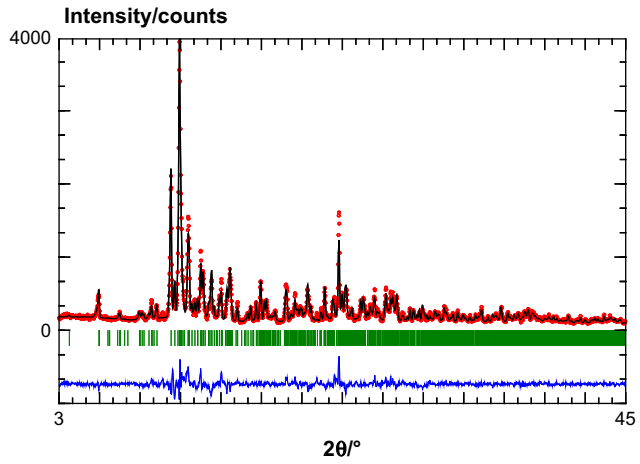

Fig. 4. Measured and calculated X-ray powder diffraction patterns of α-$AgFe_2(MoO_4)_3$, together with their difference curve (room temperature, Mo-Kα_1 radiation).

2.7. Powder diffraction data analysis

All diffraction patterns have been analyzed by full-profile Rietveld refinements, using the software package WinPLOTR [12].

2.8. Mössbauer spectroscopy

A sample of α-$AgFe_2(MoO_4)_3$ was carefully powdered and prepared as a Mössbauer absorber with 5 mg Fe/cm^2 and a diameter of 7 mm by embedding the sample homogeneously in an epoxy glue with good thermal conductivity and fixing it in a copper ring sandwiched by aluminium foils of excellent purity. The absorber was mounted in a conventional Mössbauer device (Halder Elektronik GmbH) with constant acceleration and was exposed to a nominal 50 mCi source of ^{57}Co in Rh (Wissel GmbH). The transmitted intensities were stored in a multichannel analyzer with 1024 channels and subsequently folded to 510 channels in order to improve statistics. For a good resolution and peak/background ratio comparably high counting rates were chosen. An α-Fe

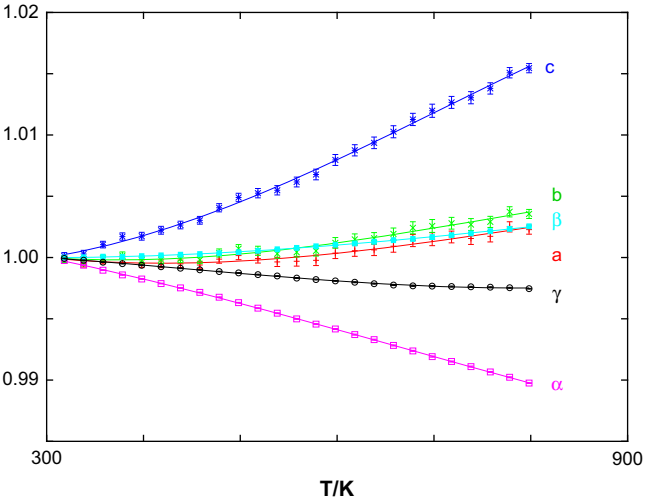

Fig. 5. Relative changes of lattice parameters, normalized to their values at 300 K (*c*: blue, *α*: purple). (For interpretation of the references to colour in this figure legend, the reader is referred to the web version of this article.)

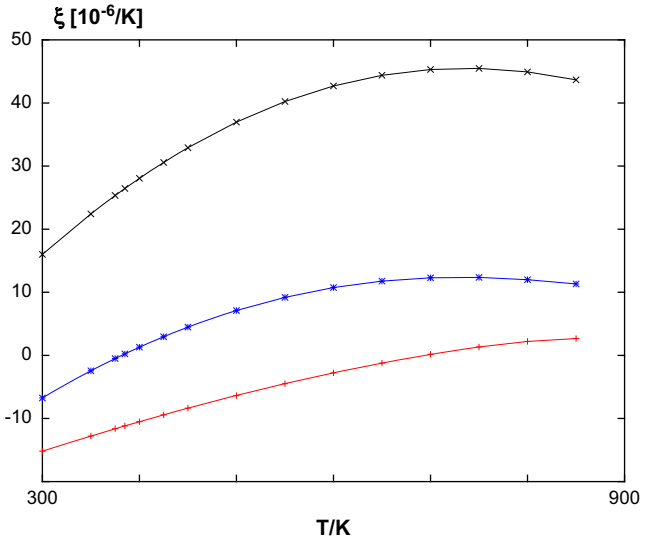

Fig. 6. Principal values ξ_i, $i = 1, 2, 3$ of the differential linear thermal expansion tensor.

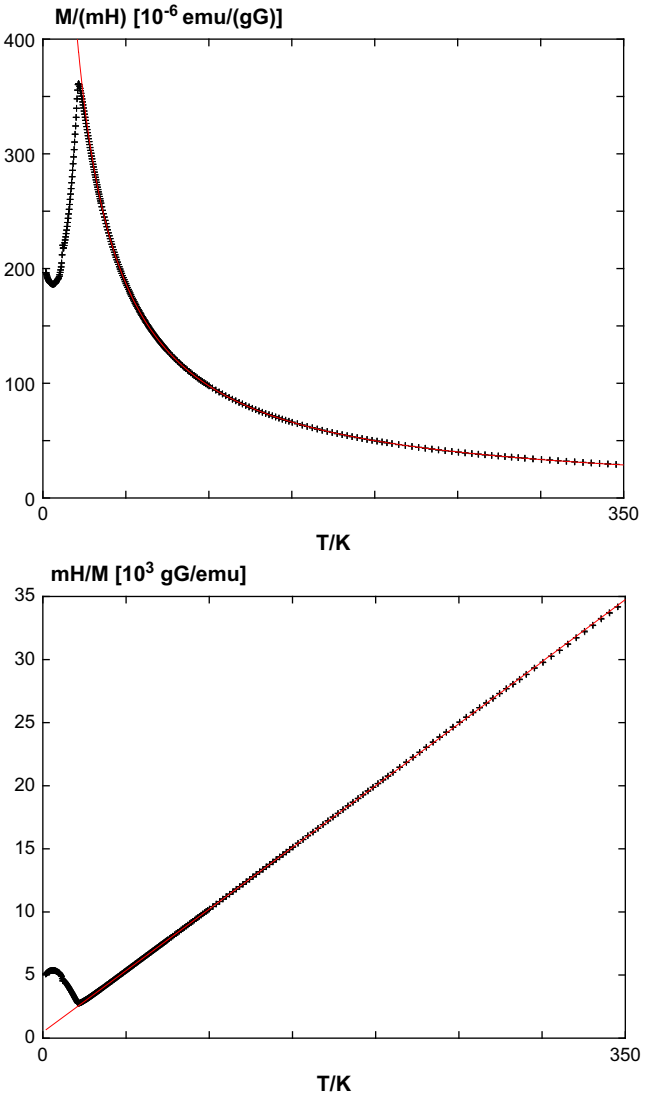

Fig. 7. Temperature dependence of magnetization (top) and its inverse (bottom), measured with an applied field of 50 Oe. The drawn lines correspond to a Curie–Weiss fit.

spectrum was recorded with the spectra in order to determine the calibration factor; and the velocity scale was subsequently recalculated from channels into mm/s. A temperature-calibrated self-constructed Mössbauer furnace and a gas-flow cryostat (Leybold GmbH) were used for the temperature dependent measurements. The obtained Mössbauer spectra (Fig. 9) were fitted with the conventional refinement routine MOESALZ [13] and decomposed into several subspectra. The corresponding parameters are summarized in Table 5 and have the following meaning: isomer-shift IS relative to α-Fe [mm/s] at room temperature, half width Γ of the lines with Lorentzian shape [mm/s], quadrupole splitting QS [mm/s] = ½ $eQV_{zz}(1+\eta^2/3)^{1/2}$ with V_{zz} as the z-component of the electric field gradient (efg), Q = nuclear quadrupole moment and η = asymmetry parameter. A [%] is the relative amount of the specific subspectrum, determined from the peak areas. The convergence of the iteration and the χ^2-value (goodness-of-fit parameter) served as an indication of the quality of the refinement.

3. Results and discussion

3.1. Crystal structure

α-$AgFe_2Mo_3O_{12}$ is isostructural to α-$NaFe_2(MoO_4)_3$ [1], and structure parameters and selected bond lengths at 104 K are given in Tables 2 and 3 (300 K data and further information is provided in the Supplementary CIFs). The structure is built up from a network

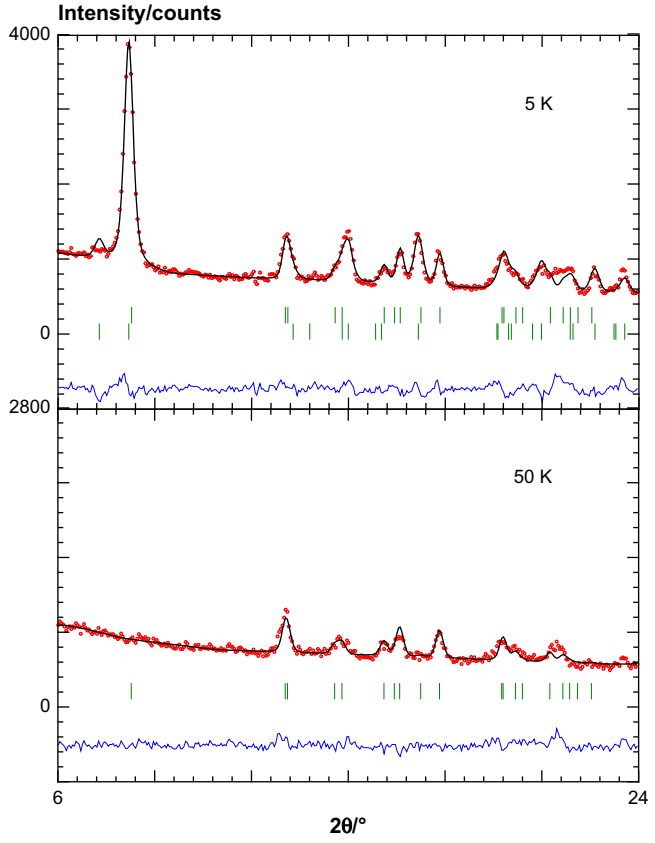

Fig. 8. Low-angle sections of the neutron diffraction patterns, $\lambda = 1.5481(1)$ Å. Observed data are points in red, the drawn lines in black are profiles, calculated by the Rietveld method and the blue lines correspond to the difference between observed and calculated intensities. The green lines mark the calculated positions of the Bragg peaks, at 50 K only the nuclear contributions and at 5 K by the second line below also the magnetic Bragg peaks according to $\mathbf{k} = (0,½,½)$. (For interpretation of the references to colour in this figure legend, the reader is referred to the web version of this article.)

of [FeO_6]-octahedra and [MoO_4]-tetrahedra as shown in Figs. 1–3. For clarity the structure is displayed by constituting layers A and B parallel to the *ab*-plane with the sequence A–B–B′–A–B–B′–… along the *c*-direction, where B′ is obtained from B by inversion symmetry. All [MoO_4]-tetrahedra are isolated from each other, so that this compound belongs to the class of ortho(oxo-)molybdates. Therefore, this phase is labelled α-$AgFe_2(MoO_4)_3$ in agreement with the notation for the $NaFe_2Mo_3O_{12}$ phases, although no metastable β-phase has been observed for $AgFe_2Mo_3O_{12}$ so far in contrast to $NaFe_2Mo_3O_{12}$ [1,2]. Ag-ions are coordinated by four oxygens (2.263–2.508 Å), shown as bonds in Figs. 1 and 3 instead of polyhedra for clarity. The distance to the next nearest oxygen is 2.998 Å, so that only the four nearest oxygens have been included. The pronounced anisotropy of the thermal displacement of the Ag ions, especially at room temperature, might be an indication for a thermally activated Ag-ion mobility, which could also contribute to the rather high residual difference electron density at 300 K very close to the Ag-site.

The average iron–oxygen distances are ⟨Fe(1)–O⟩ = 2.073 Å and ⟨Fe(2)–O⟩ = 2.018 Å at 300 K. These values differ significantly for both sites and are between typical values for Fe^{2+} (2.00 Å) and Fe^{3+} (2.13 Å) in high-spin configurations with coordination number six. The difference between the average bond lengths becomes larger at lower temperatures: ⟨Fe(1)–O⟩ = 2.081 Å and ⟨Fe(2)–O⟩ = 2.005 Å are determined from single-crystal X-ray diffraction at 104 K and ⟨Fe(1)–O⟩ = 2.089 Å and ⟨Fe(2)–O⟩ = 1.977 Å from neutron powder diffraction at 50 K.

An X-ray diffraction pattern from a polycrystalline sample is shown in Fig. 4. The calculated profile is based on the atomic coordinates from single-crystal X-ray diffraction. Only overall parameters (like lattice parameters, scale factor etc., but no atomic coordinates) have been refined by the Rietveld method. Two weak reflections are observed in addition to those from α-$AgFe_2(MoO_4)_3$. They can be assigned to a tiny amount of MoO_3, less than 1% weight to weight, which was not included in the calculated diffraction pattern.

3.2. Thermal expansion

The temperature dependences of the lattice parameters are shown as relative changes in Fig. 5. Analysis of thermal behaviour revealed a strong anisotropy of thermal expansion, which is most pronounced along the *c*-axis, while the angle α decreases with increasing temperature. In structures with triclinic symmetry no fixed orientations exist between the principal-axes system of the differential linear thermal expansion tensor and the crystal-axes system. The principal values, shown in Fig. 6, have been determined from the temperature dependence of the lattice parameters as described in [14]. No anomalies are observed in their temperature dependence, and the orientation

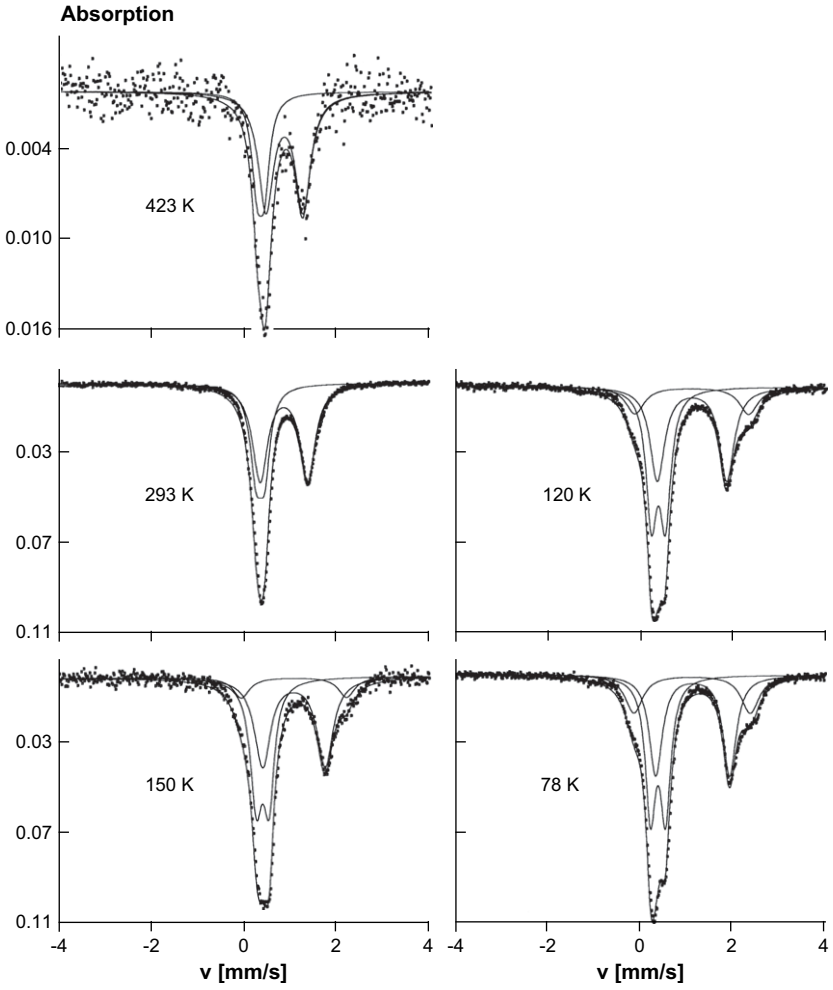

Fig. 9. Mössbauer spectra at different temperatures, together with the fitted subspectra, shown as drawn lines.

Table 4
Super- and supersuperexchange paths in α-$AgFe_2(MoO_4)_3$.

	F/AF	Geometry of the Fe–O–Fe superexchange path, bond lengths in Å							d [Å]
J_A	↑↑	Fe(1)	– 2.110	99.97° O(8)	– 2.107			Fe(1)′ [1 0]	3.230
	F/AF	Geometry of Fe–O–O–Fe supersuperexchange paths, bond lengths in Å							d [Å]
J_1	↑↓	Fe(1)	– 2.081	139.99° O(5)	Ag 3.267	140.49° O(1)	– 2.008	Fe(2)′[10$\bar{1}$]	6.923
J_2	↑↑	Fe(1)	– 2.110	159.90° O(8)	Mo(3) 2.863	161.73° O(7)	– 2.044	Fe(1)[100]	6.922
J_3	↑↑	Fe(2)	– 2.029	163.66° O(3)	Mo(1) 2.945	165.67° O(4)	– 2.011	Fe(2)[100]	6.922
J_4	↑↓	Fe(1)	– 2.078	156.96° O(10)	Mo(3) 2.888	154.61° O(8)	– 2.107	Fe(1)[010]	6.917
J_5	↑↓	Fe(2)	– 2.014	169.93° O(12)	Mo(2) 2.972	165.52° O(2)	– 1.975	Fe(2)[010]	6.917
J_6	↑↓	Fe(1)	– 2.065	154.81° O(6)	Mo(1) 2.799	154.60° O(1)	– 2.008	Fe(2)[0$\bar{1}$1]	6.711
J_7	↑↓	Fe(1)	– 2.044	137.52° O(7)	Mo(3) 2.859	132.71° O(10)	– 2.078	Fe(1)′	5.804
J_{8a}	↑↑	Fe(2)	– 2.014	124.77° O(12)	Mo(2) 2.917	132.99° O(5)	– 2.081	Fe(1)[010]	5.588
J_{8b}	↑↑	Fe(2)	– 1.997	130.41° O(9)	Mo(3) 2.927	113.84° O(8)	– 2.107	Fe(1)[010]	5.588
J_{9a}	↑↑	Fe(1)	– 2.044	120.74° O(7)	Mo(3) 2.845	140.82° O(9)	– 1.997	Fe(2)′	5.561
J_{9b}	↑↑	Fe(1)	– 2.065	140.61° O(6)	Mo(1) 2.803	119.52° O(4)	– 2.011	Fe(2)′	5.561
J_{10a}	↑↓	Fe(1)	– 2.081	153.36° O(5)	Mo(2) 2.879	109.50° O(2)	– 1.975	Fe(2)	5.547
J_{10b}	↑↓	Fe(1)	– 2.078	106.28° O(10)	Mo(3) 2.905	158.72° O(9)	– 1.997	Fe(2)	5.547
J_{10c}	↑↓	Fe(1)	– 2.081	125.37° O(5)	Ag 4.109	72.50° O(3)	– 2.029	Fe(2)	5.547
J_{11}	↑↓	Fe(1)	– 2.078	156.96° O(10)	Mo(3) 2.888	100.29° O(8)	– 2.110	Fe(1)′[100]	5.448
J_{12a}	↑↑	Fe(1)	– 2.065	124.44° O(6)	Mo(1) 2.804	125.14° O(3)	– 2.029	Fe(2)′[100]	5.443
J_{12b}	↑↑	Fe(1)	– 2.110	113.84° O(8)	Mo(3) 2.927	130.41° O(9)	– 1.997	Fe(2)′[100]	5.443
J_{13}	↑↑	Fe(1)	– 2.107	99.19° O(8)	Mo(3) 2.863	161.73° O(7)	– 2.044	Fe(1)′[0$\bar{1}$0]	5.355
J_{14}	↑↑	Fe(2)	– 2.029	95.76° O(3)	Ag 4.128	89.53° O(1)	– 2.008	Fe(2)′[10$\bar{1}$]	5.148
J_{15}	↑↓	Fe(2)	– 2.008	96.85° O(1)	Mo(1) 2.969	131.00° O(4)	– 2.011	Fe(2)′[01$\bar{1}$]	5.084
J_{16}	↑↓	Fe(2)	– 2.008	108.31° O(1)	Mo(1) 3.028	107.34° O(3)	– 2.029	Fe(2)′[11$\bar{1}$]	4.957

of the principal-axes systems changes only slightly with respect to the crystal-axes system.

3.3. Magnetic properties

Antiferromagnetic ordering is indicated by a sharp maximum in the temperature dependence of magnetization at $T = 21.5(5)$ K, see Fig. 7. At higher temperatures the magnetization obeys a Curie–Weiss law $M(T) = C/(T - \theta)$ with $\theta = -5$ K, and a least-squares fit to the data between 50 and 350 K is shown as drawn lines. A paramagnetic moment of 5.36(1) μ_B per Fe-ion is calculated from the Curie constant C.

Antiferromagnetic ordering is also reflected in additional magnetic Bragg peaks in neutron powder diffraction patterns, see Fig. 8 for a comparison between data sets recorded at 50 K (above T_N) and at 5 K (below T_N). The additional magnetic reflections can be indexed, based on the propagation vector $\mathbf{k} = (0,½,½)$. Only one magnetic structure model matched the observed intensities. Accordingly, the magnetic moments are collinear aligned in the *ab*-plane $\mu = (\mu_x,\mu_y,0)$ with $\mu_x = 4.2(1)\,\mu_B$, $\mu_y = -2.7(2)\,\mu_B$ and an absolute value of 4.6(1) μ_B per Fe-ion. The four magnetic moments on the two Fe(1) positions at $(x_1,y_1,z_1) = (-0.1819, 0.1751, -0.4939)$ and $(-x_1, -y_1, -z_1)$ and on the two Fe(2) positions at $(x_2,y_2,z_2) = (-0.2277, -0.2303, 0.1052)$ and $(-x_2, -y_2, -z_2)$ are aligned as $+ - - +$ with respect to each other. All other magnetic moments are generated by the propagation vector **k**. The magnetic moments are shown as arrows in Figs. 1–3. Small canting angles, an additional μ_z-component or minor differences between the moments on the Fe(1)- and Fe(2)-sites cannot be ruled out, but taking them into account does not result in a significant improvement between observed and calculated magnetic intensities. The unconstrained magnetic moments for the Fe(1)- and Fe(2) sites converge to 4.5(2) μ_B and 4.8(2) μ_B, respectively, which is not significantly different, but points into the direction of the proposed Fe^{2+} state for Fe(1) and Fe^{3+} for Fe(2). To obtain more information about the formal oxidation states of Fe Mössbauer spectroscopy was applied. The observed spectra are shown in Fig. 9 for different temperatures, the derived parameters are summarized in Table 5. The data at room temperature and 423 K are in agreement with an interpretation of an intermediate oxidation state for both Fe-sites, i.e. a shared delocalized electron. This is evident from the slightly too high value of the isomer shift for Fe^{3+} on one crystallographic site and the much too low value of the isomer shift for Fe^{2+} on the other. Between room temperature and 150 K a change in the electronic configuration is revealed by the splitting of one subspectrum into two (II + III, Table 5). Below 150 K these both subspectra reach a value for the isomer shift which is common for Fe^{2+}, while the other subspectrum (I) is rather unaffected by cooling. The relative amount, corresponding to subspectrum III increases at low temperatures, while the sum of subspectra II and III remains constant below 150 K within experimental uncertainty. These findings support the proposed change in the electronic configurations of the Fe ions, based on the changes in the Fe–O distances with temperature as observed by single-crystal X-ray and neutron powder diffraction. However, Mössbauer spectroscopy probes the local magnetic hyperfine field and reveals a more complex process than just a charge ordering of electrons, delocalized between the two Fe sites at elevated temperature on distinct Fe^{2+} and Fe^{3+} sites at low temperature. The constant slope in the temperature dependence of inverse magnetization (Fig. 7) corresponds to a constant average paramagnetic moment per Fe-ion over the whole temperature range above T_N. Therefore, the changes in the

Table 5
Mössbauer parameters of α-$AgFe_2(MoO_4)_3$ for different temperatures. Up to 3 subspectra have been used to fit the observed spectra. The isomer-shift IS is determined with an experimental error of 0.01 mm/s.

T [K]	Subspectrum	IS [mm/s]	Γ [mm/s]	QS [mm/s]	A [%]	χ^2
423	I	0.46	0.28	0.15	33.4	0.45
	II	0.97	0.39	0.79	66.6	
	–	–	–	–	–	
293	I	0.50	0.30	0.17	38.6	1.18
	II	1.01	0.39	1.02	61.4	
	–	–	–	–	–	
150	I	0.52	0.30	0.26	42.9	0.37
	II	1.20	0.42	1.34	46.1	
	III	1.21	0.43	2.26	11.0	
120	I	0.52	0.28	0.29	42.4	0.60
	II	1.24	0.38	1.49	41.9	
	III	1.23	0.49	2.44	15.7	
78	I	0.52	0.27	0.31	41.1	0.87
	II	1.27	0.34	1.58	38.8	
	III	1.25	0.47	2.50	20.1	

local electronic configurations do not effect the average paramagnetic moment. Both the averaged ordered magnetic moment of 4.6(1) μ_B and the averaged paramagnetic moment of 5.36(1) μ_B per Fe-ion are between typical values for HS-Fe^{2+} (spin-only: 4 μ_B and 4.9 μ_B) and HS-Fe^{3+} (5 μ_B and 5.92 μ_B).

The observed magnetic structure reveals the dominant magnetic couplings. In Table 4 the geometry of the superexchange path J_A and all supersuperexchange paths via two oxygens, belonging to the same coordination polyhedra of one diamagnetic ion, are listed. The supersuperexchange couplings Fe–O–O–Fe are ordered with decreasing Fe–Fe distances, because the larger angles Fe–O–O and O–O–Fe along these paths are expected to result in stronger antiferromagnetic couplings. This empirical rule has been observed for numerous supersuperexchange couplings, e.g. between Mn^{2+} ions in $MnWO_4$ [15] and α-$MnMoO_4$ [16], Cu^{2+} ions in $CuMoO_4$-III [17] and Fe^{3+} ions in $Fe_2(MoO_4)_3$ [18]. In all these cases, the superexchange couplings are not the dominant magnetic interactions, but those supersuperexchange couplings with the largest angles. If only supersuperexchange couplings via two oxygens of one common $[MoO_4]$-tetrahedron are considered, magnetic structures are predicted for the quaternary Na–Fe–Mo–O phases, which are not in agreement with the observed magnetic Bragg peaks [2]. As in the case of α-$NaFe_2(MoO_4)_3$, a magnetic unit cell with a doubling of the *a*- and *b*-axes would be expected for α-$AgFe_2(MoO_4)_3$ in contrast to the observed propagation vector $\mathbf{k} = (0,½,½)$. Note that not all supersuperexchange couplings Fe–O–O–Fe with an averaged Fe–O–O and O–O–Fe angle above 135°, this is J_1,…, J_7 in Table 4, can result in antiferromagnetic pairs simultaneously, so that competing interactions exist. However, it is very surprising that the supersuperexchange paths J_2 and J_3 correspond to pairs with parallel magnetic moments, in contrast to the expected rather strong antiferromagnetic couplings. This might be a reflection of complex magnetic interactions due to different oxidations states on both Fe sites at low temperatures. The explanation of the observed magnetic structure requires relevant magnetic interactions along exchange paths, including Ag–O bonds. A long-range (~10 Å) "bridging" effect of magnetic couplings by $[NaO_6]$-octahedra has recently been reported for the similar systems $NaFe(WO_4)_2$ and $NaCr(WO_4)_2$ [19].

At present it is not clear, which mechanism is responsible for the magnetic interactions in α-$AgFe_2(MoO_4)_3$. Most probably the couplings via Ag–O bonds and the non-integer average formal oxidation state of $Fe^{2.5+}$ (assuming Mo^{6+}) with a kind of Fe(II)–Fe(III) exchange are of primary importance. The magnetic structures of more such network structures need to be determined in order to elucidate the magnetic interactions and to allow for an explanation of the rather high magnetic ordering temperature in the light of the long Fe–Fe distances. The results support the relevance of long-range magnetic exchange interactions mediated by AgO-polyhedra as already previously concluded for NaO-polyhedra in closely related compounds [2,18]. The three times higher temperature of the maximum in the temperature dependence of magnetization $M(T)$ for α-$AgFe_2(MoO_4)_3$ (21.5 K) in comparison with isostructural α-$NaFe_2(MoO_4)_3$ (7 K) gives evidence for a stronger coupling effect by Ag ions than via Na ions.

Acknowledgments

This work was supported by *Deutscher Akademischer Austauschdienst* (DAAD) and *Deutsche Forschungsgemeinschaft* (DFG EH183/2). The neutron powder diffractometer SPODI is funded by the *Bundesministerium für Bildung und Forschung* (03FU7DAR).

Appendix. Supplementary data

Supplementary data associated with this article can also be found in the online version, at doi:10.1016/j.solidstatesciences.2009.03.006.

References

[1] E. Muessig, K.G. Bramnik, H. Ehrenberg, Acta Crystallogr., B 59 (2003) 611–616.
[2] H. Ehrenberg, E. Muessig, K.G. Bramnik, P. Kampe, T. Hansen, Solid State Sci. 8 (2006) 813–820.
[3] R.F. Klevtsova, Dokl. Akad. Nauk. SSSR 221 (1975) 1322–1325.
[4] K.G. Bramnik, E. Muessig, H. Ehrenberg, J. Solid State Chem. 176 (2003) 192–197.
[5] P. Klevtsov, A. Perepelitsa, Russ. J. Inorg. Chem. 29 (1984) 1292.
[6] G.M. Sheldrick, Acta Crystallogr., A 46 (1990) 467–473.
[7] G.M. Sheldrick, SHELXL97: Program for the Refinement of Crystal Structures, University of Göttingen, Germany, 1997.
[8] Stoe & Cie, X-STEP32, Stoe & Cie GmbH, Darmstadt, Germany, 2000.
[9] M. Knapp, C. Baehtz, H. Ehrenberg, H. Fuess, J. Synchrotron Radiat. 11 (2004) 328–334.
[10] M. Knapp, V. Joco, C. Baehtz, H.H. Brecht, A. Berghaeuser, H. Ehrenberg, H. von Seggern, H. Fuess, Nucl. Instrum. Methods A 521 (2004) 565–570.
[11] M. Hoelzel, A. Senyshyn, R. Gilles, H. Boysen, H. Fuess, Neutron News 18(4) (2007) 23–26.
[12] T. Roisnel, J. Rodriguez-Carvajal, Mater. Sci. Forum 378–381 (2001) 118–123.
[13] W. Lottermoser, P. Kaliba, K. Forcher, G. Amthauer, Unpublished, University of Salzburg, Austria, 1993.
[14] P. Paufler, T. Weber, Eur. J. Mineral. 11 (1999) 721–730.
[15] H. Ehrenberg, H. Weitzel, H. Fuess, B. Hennion, J. Phys.: Condens. Matter 11 (1999) 2649–2659.
[16] H. Ehrenberg, B. Schwarz, H. Weitzel, J. Magn. Magn. Mater. 305 (2006) 57–62.
[17] H. Ehrenberg, M. Wiesmann, J. Garcia-Jaca, H. Weitzel, H. Fuess, J. Magn. Magn. Mater. 182 (1998) 152–160.
[18] H. Ehrenberg, K.G. Bramnik, E. Muessig, T. Buhrmester, H. Weitzel, C. Ritter, J. Magn. Magn. Mater. 261 (2003) 353–359.
[19] L. Nyam-Ochir, H. Ehrenberg, A. Buchsteiner, A. Senyshyn, H. Fuess, D. Sangaa, J. Magn. Magn. Mater. 320 (2008) 3251–3255.